Science Advances
AAAS

Supplementary Materials for

Structural basis for target discrimination and activation by Cas13d

Chia-Wei Chou *et al.*

Corresponding author: Chia-Wei Chou, alvincwchou@gmail.com; Ilya J. Finkelstein, ilya@finkelsteinlab.org

Sci. Adv. **12**, eaec4221 (2026)
DOI: 10.1126/sciadv.aec4221

This PDF file includes:

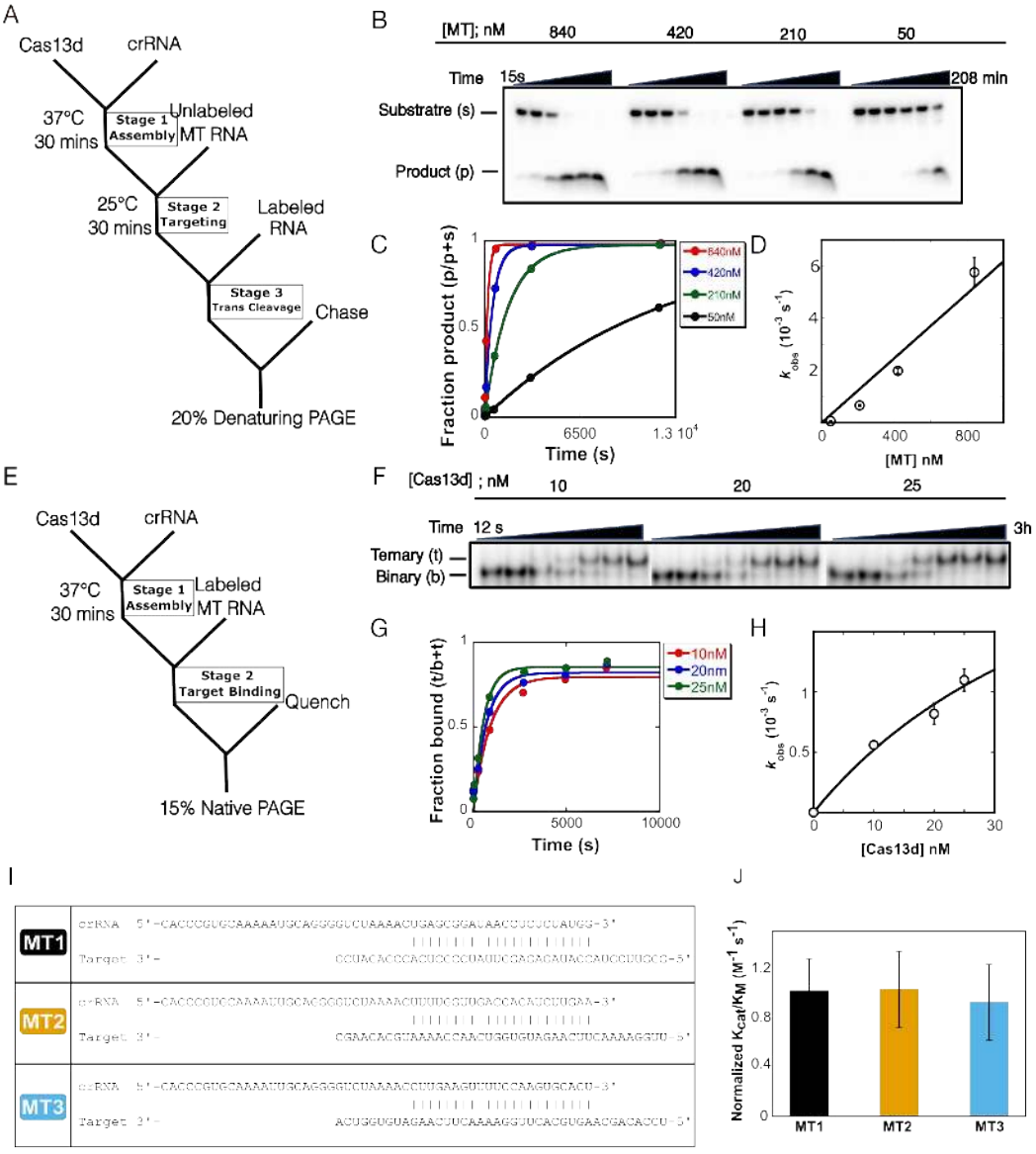
A
Cas13d
crRNA
37°C
30 mins
Stage 1
Assembly
Unlabeled
MT RNA
25°C
30 mins
Stage 2
Targeting
Labeled
RNA
Stage 3
Trans Cleavage
Chase
20% Denaturing PAGE
B
[MT]; nM
840
420
210
50
Time
15s
208 min
Substratre (s)
Product (p)
C
Fraction product (p/p+s)
Time (s)
840nM
420nM
210nM
50nM
D
[MT] nM
E
Cas13d
crRNA
37°C
30 mins
Stage 1
Assembly
Labeled
MT RNA
Stage 2
Target Binding
Quench
15% Native PAGE
F
[Cas13d] ; nM
10
20
25
Time
12 s
3h
Ternary (t)
Binary (b)
G
Fraction bound (t/b+t)
Time (s)
10nM
20nm
25nM
H
[Cas13d] nM
I
MT1
MT2
MT3
J
MT1
MT2
MT3

Figure S1: Quantitative substrate cleavage and binding kinetics. (A) Schematic of the *trans* cleavage assay with a 10 nt substrate. Stage 1: Cas13d assembles with crRNA. Stage 2: the assembled complex binds to a matched target. Stage 3: activated Cas13d cleaves the radiolabeled *trans* substrate. (B) Representative gel with varying concentrations of the activated Cas13d complex. The reaction initiates when the substrate RNA is added, and is quenched at various time points (15 s, 30 s, 105 s, 12 min, 55 min, 208 min). (C) Quantification of cleavage gels were fit to pseudo-first-order rate equations (solid lines) for the indicated activated RNP concentrations. (D) Second-order rate and maximal first-order rate constants from a hyperbolic fit to the observed rate constants from (C). (E) Schematic of the binding assay for Cas13d using a matched target RNA (40 nt). Stage 1: Cas13d assembles with crRNA. Stage 2: the assembled complex binds to the fully matched target. (F) Representative gel showing time courses for Cas13d binding to trace radiolabeled MT RNA. Time points: 12 s, 90 s, 9 min, 29 min, 1.5 h, 3 h. (G) Time-course data from the gel with fits to pseudo-first-order rate equations. (H) Second-order and maximal first-order rate constants from a hyperbolic fit to the data from (G). Results are presented as the mean with SEM from three independent experiments. (I) Basepair composition does not impact Cas13d trans cleavage rates. We measured the trans cleavage activity for three matched pair sequences. Cas13d was activated with fully matched crRNA–target pairs, and trans cleavage was measured using a radiolabeled reporter substrate, as described above. (J) Rates (normalized $k_{\text{cat}}/K_{\text{M}}$ to MT1) were comparable across all three matched pairs, indicating that Cas13d cleavage rates are not dependent on base-pair composition. Error bars represent SD from three independent replicates.

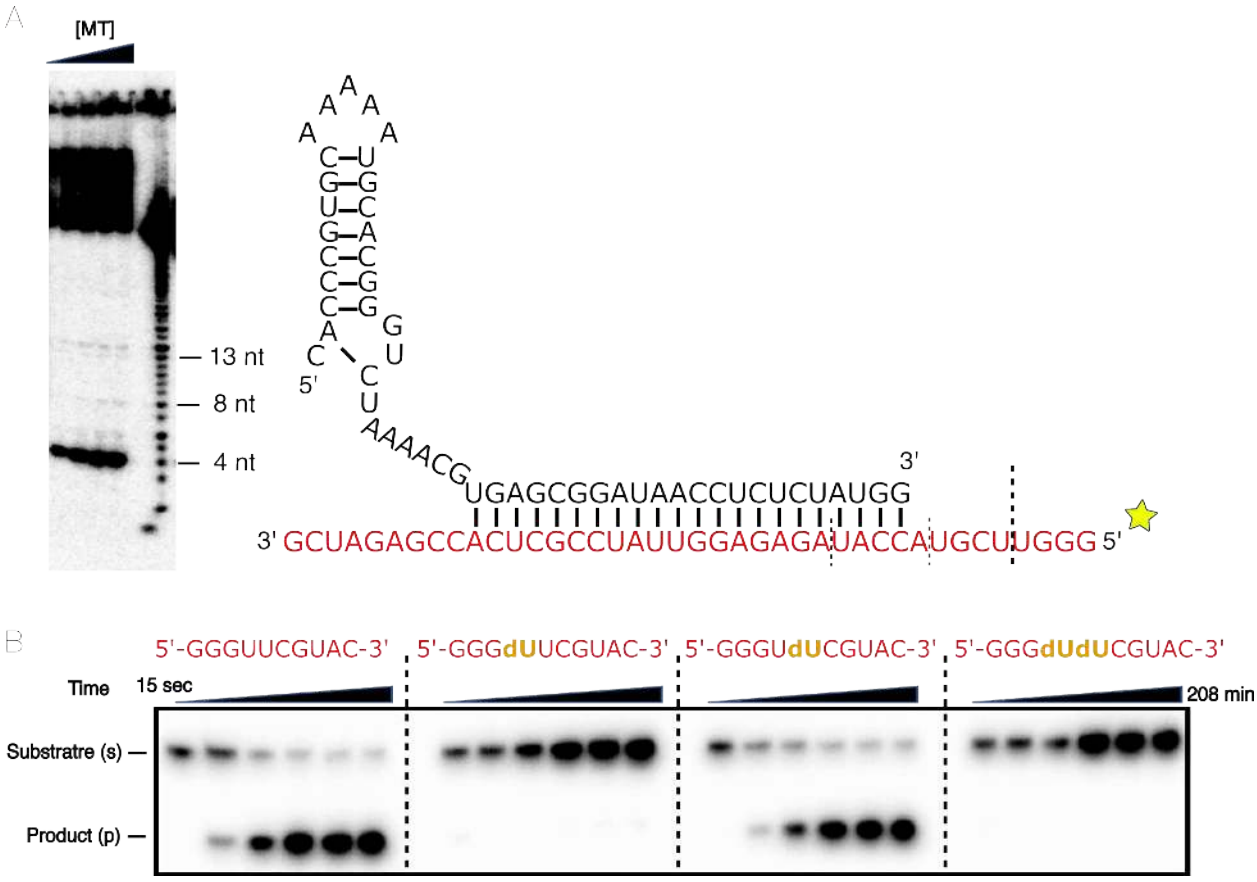

Figure S2: Cas13d cleaves between UU dinucleotides. (A) Cleavage of a radiolabeled matched target (MT) RNA (red) by Cas13d activated with an unlabeled MT RNA. Ladder: alkaline-hydrolyzed MT RNA. The cleavage products are marked by dashed lines. (B) Cleavage of a 10 nt *trans* substrate by activated Cas13d. Full cleavage requires a 5'-U ribose nucleotide; a deoxyribose sugar in this position inhibits all cleavage. The reaction is initiated by the addition of substrate RNA and quenched at different time points (15 s, 8 min, 30 min, 1 h, 2.5 h, 3.4 h)

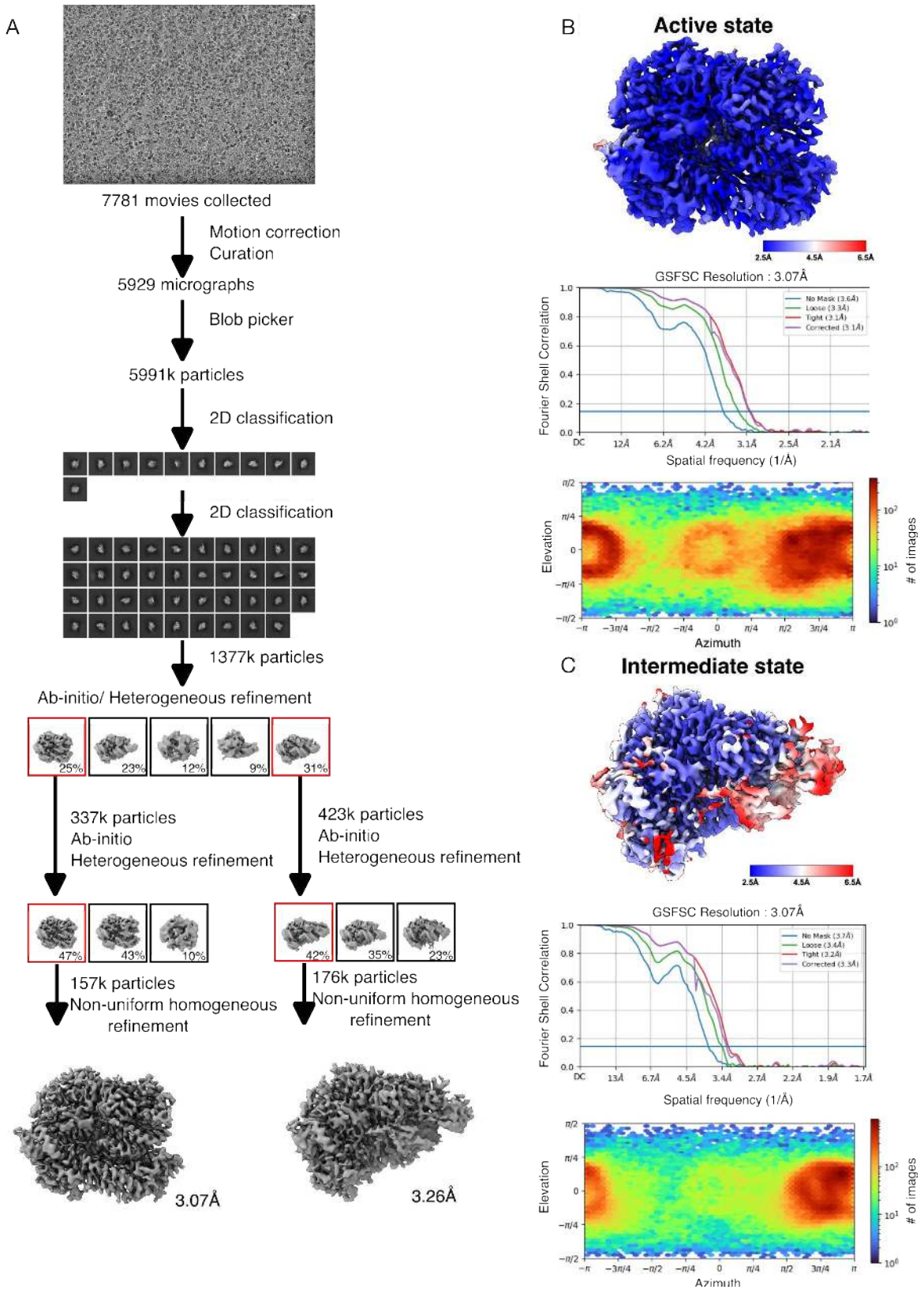
A
7781 movies collected
Motion correction
Curation
5929 micrographs
Blob picker
5991k particles
2D classification
2D classification
1377k particles
Ab-initio/ Heterogeneous refinement
25%
23%
12%
9%
31%
337k particles
Ab-initio
Heterogeneous refinement
423k particles
Ab-initio
Heterogeneous refinement
47%
43%
10%
42%
35%
23%
157k particles
Non-uniform homogeneous refinement
176k particles
Non-uniform homogeneous refinement
3.07Å
3.26Å
B
Active state
2.5Å
4.5Å
6.5Å
GSFSC Resolution : 3.07Å
Fourier Shell Correlation
Spatial frequency (1/Å)
Elevation
Azimuth
# of images
C
Intermediate state
2.5Å
4.5Å
6.5Å
GSFSC Resolution : 3.07Å
Fourier Shell Correlation
Spatial frequency (1/Å)
Elevation
Azimuth
# of images

Figure S3: Cryo-EM data collection, analysis, and resolution estimation of active state and intermediate state of Cas13d-crRNA-matched-target RNA ternary complex (A) Workflow of data collection and analysis of Cas13d-crRNA-matched-target RNA ternary complex(57, 61). (B) Refined map of the active state of Cas13d-crRNA-matched-target complex colored by local resolution (top). Fourier Shell Correlation (FSC) curves for cross-validation between two half maps of the active state of Cas13d-crRNA-matched-target RNA ternary complex. Resolutions were estimated at FSC=0.143 (middle). Euler diagrams showing orientation distributions of the particles used in the final 3D reconstruction (bottom). (C) Refined map of the intermediate state of Cas13d-crRNA-matched-target complex colored by local resolution (top). Fourier Shell Correlation (FSC) curves for cross-validation between two half maps of the intermediate state of Cas13d-crRNA-matched-target RNA ternary complex. Resolutions were estimated at FSC=0.143 (middle). Euler diagrams showing orientation distributions of the particles used in the final 3D reconstruction (bottom).

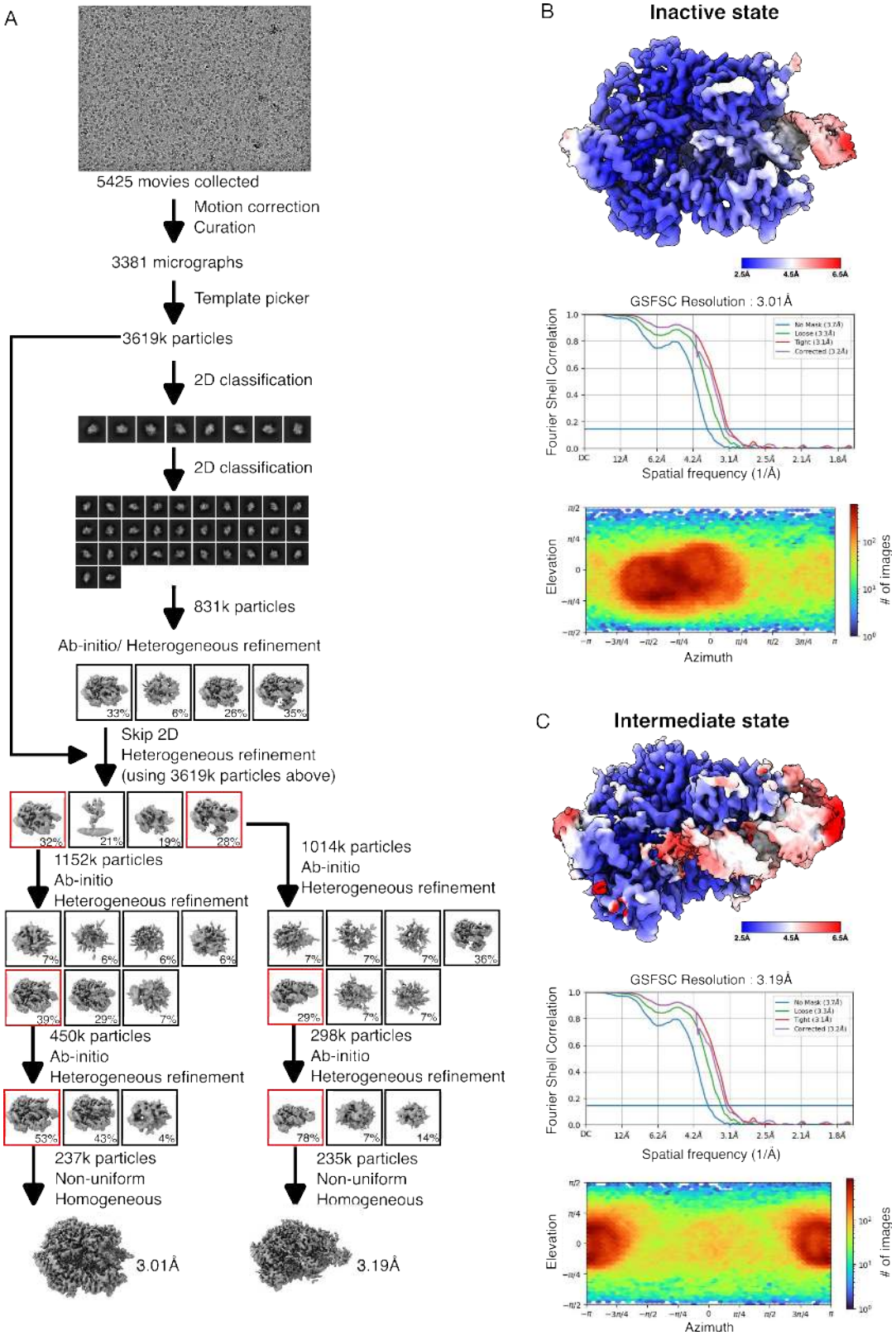
A
5425 movies collected
Motion correction
Curation
3381 micrographs
Template picker
3619k particles
2D classification
2D classification
831k particles
Ab-initio/ Heterogeneous refinement
33%
6%
26%
35%
Skip 2D
Heterogeneous refinement
(using 3619k particles above)
32%
21%
19%
28%
1152k particles
Ab-initio
Heterogeneous refinement
1014k particles
Ab-initio
Heterogeneous refinement
7%
6%
6%
6%
7%
7%
7%
36%
39%
29%
7%
29%
7%
7%
450k particles
Ab-initio
Heterogeneous refinement
298k particles
Ab-initio
Heterogeneous refinement
53%
43%
4%
78%
7%
14%
237k particles
Non-uniform
Homogeneous
235k particles
Non-uniform
Homogeneous
3.01Å
3.19Å
B
Inactive state
2.5Å
4.5Å
6.5Å
GSFSC Resolution : 3.01Å
Fourier Shell Correlation
Spatial frequency (1/Å)
Elevation
Azimuth
# of images
C
Intermediate state
2.5Å
4.5Å
6.5Å
GSFSC Resolution : 3.19Å
Fourier Shell Correlation
Spatial frequency (1/Å)
Elevation
Azimuth
# of images

Figure S4: Cryo-EM data collection, analysis, and resolution estimation of the active and intermediate Cas13d ternary complexes. (A) Workflow of data collection and analysis of Cas13d-crRNA-matched-target RNA ternary complex(57, 61).(B) Refined map of the active state of Cas13d-crRNA-matched-target complex colored by local resolution (top). Fourier Shell Correlation (FSC) curves for cross-validation between two half maps of the active state of Cas13d-crRNA-matched-target RNA ternary complex. Resolutions were estimated at FSC=0.143 (middle). Euler diagrams showing orientation distributions of the particles used in the final 3D reconstruction (bottom).(C) Refined map of the intermediate state of Cas13d-crRNA-matched-target complex colored by local resolution (top). Fourier Shell Correlation (FSC) curves for cross-validation between two half maps of the intermediate state of Cas13d-crRNA-matched-target RNA ternary complex. Resolutions were estimated at FSC=0.143 (middle). Euler diagrams showing orientation distributions of the particles used in the final 3D reconstruction (bottom).

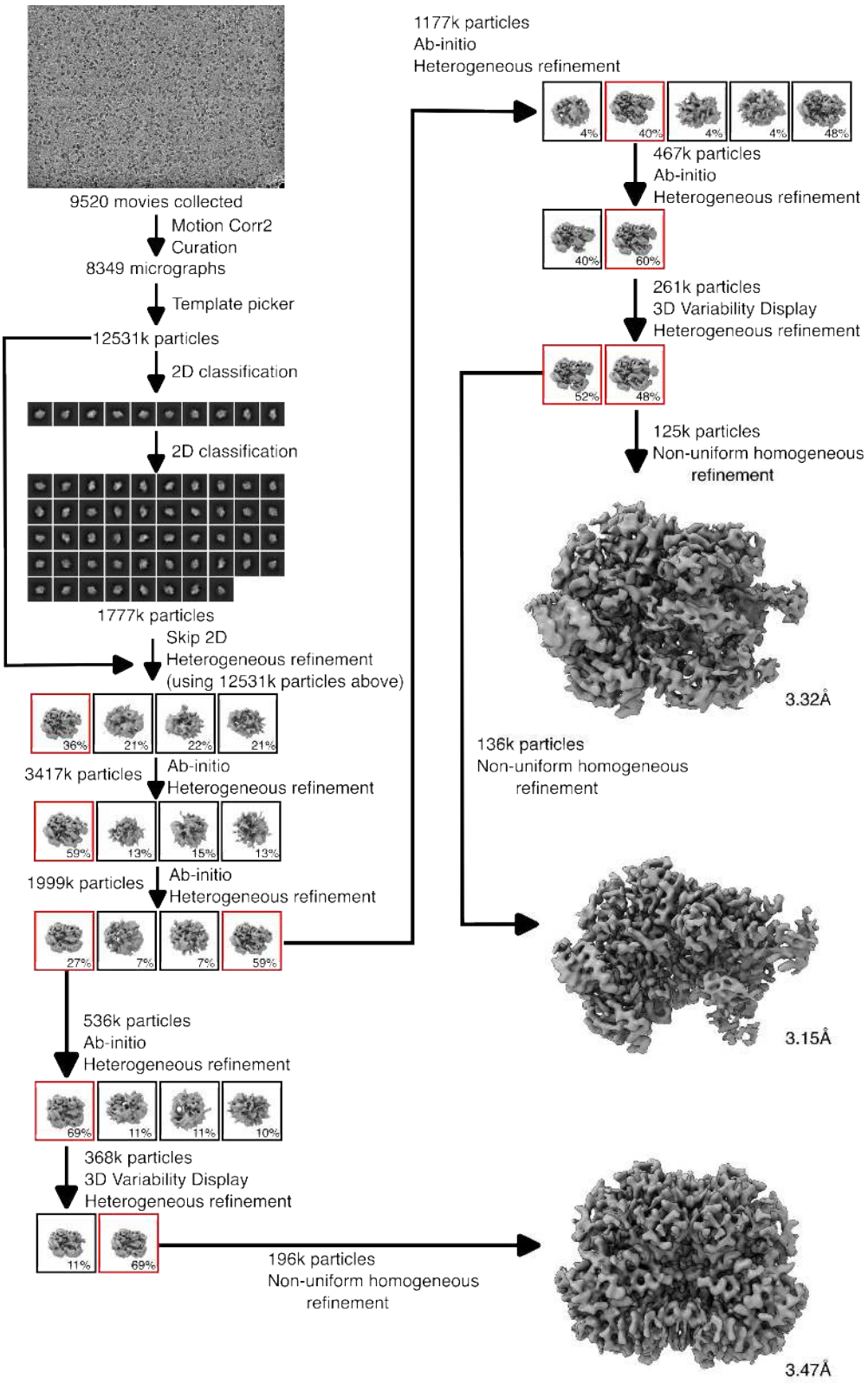

Figure S5: Cryo-EM data collection and analysis of Cas13d-crRNA-U10G-target RNA ternary complex. Workflow of data collection and analysis of Cas13d-crRNA-U10G-target RNA ternary complex(57, 61).

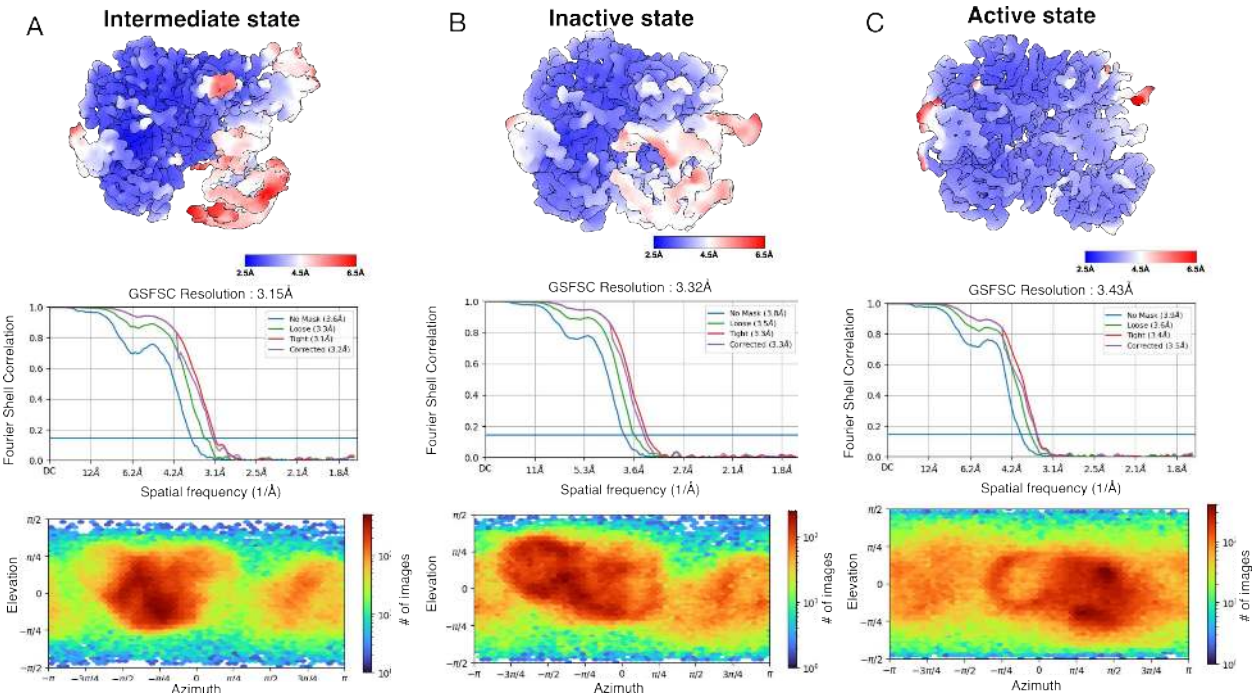

Figure S6: Cryo-EM data analysis of Cas13d-crRNA-U10G-target RNA ternary complex. Refined map of the (A) intermediate state, (B) inactive state, (C) active state of Cas13d-crRNA-U10G-target complex colored by local resolution (top). Fourier Shell Correlation (FSC) curves for cross-validation between two half maps of the active state of Cas13d-crRNA-U10G-target RNA ternary complex. Resolutions were estimated at FSC=0.143 (middle). Euler diagrams showing orientation distributions of the particles used in the final 3D reconstruction (bottom).

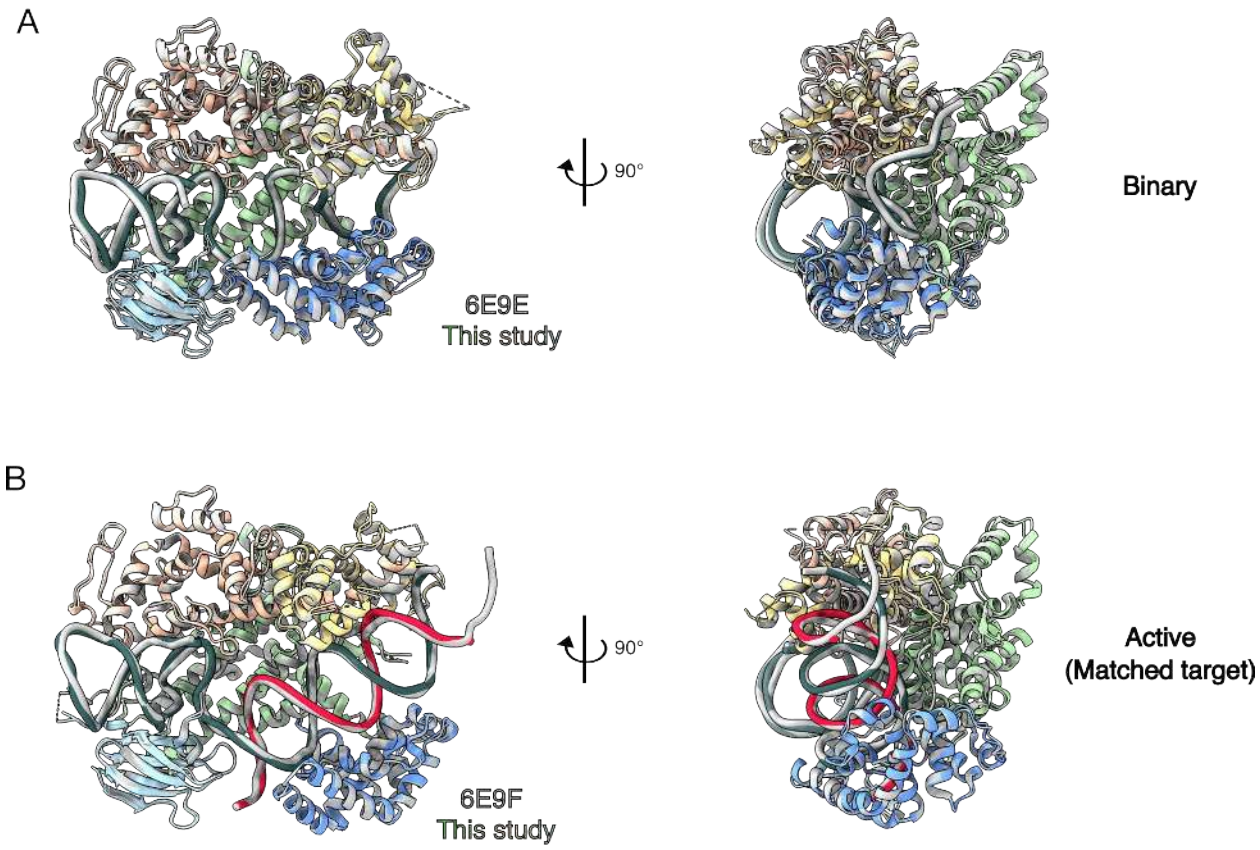

Figure S7: Comparison to published EsCas13d structures. (A) Superposition of binary EsCas13d structures. Gray: 6E9E from Zhang et al.(18). Colored: this study. The Cα-Cα-RMSD is 1.327 Å. (B) Superposition of active EsCas13d structures. Gray: 6E9F from Zhang et al.(18). Colored: this study. The Cα-Cα-RMSD is 0.700 Å.

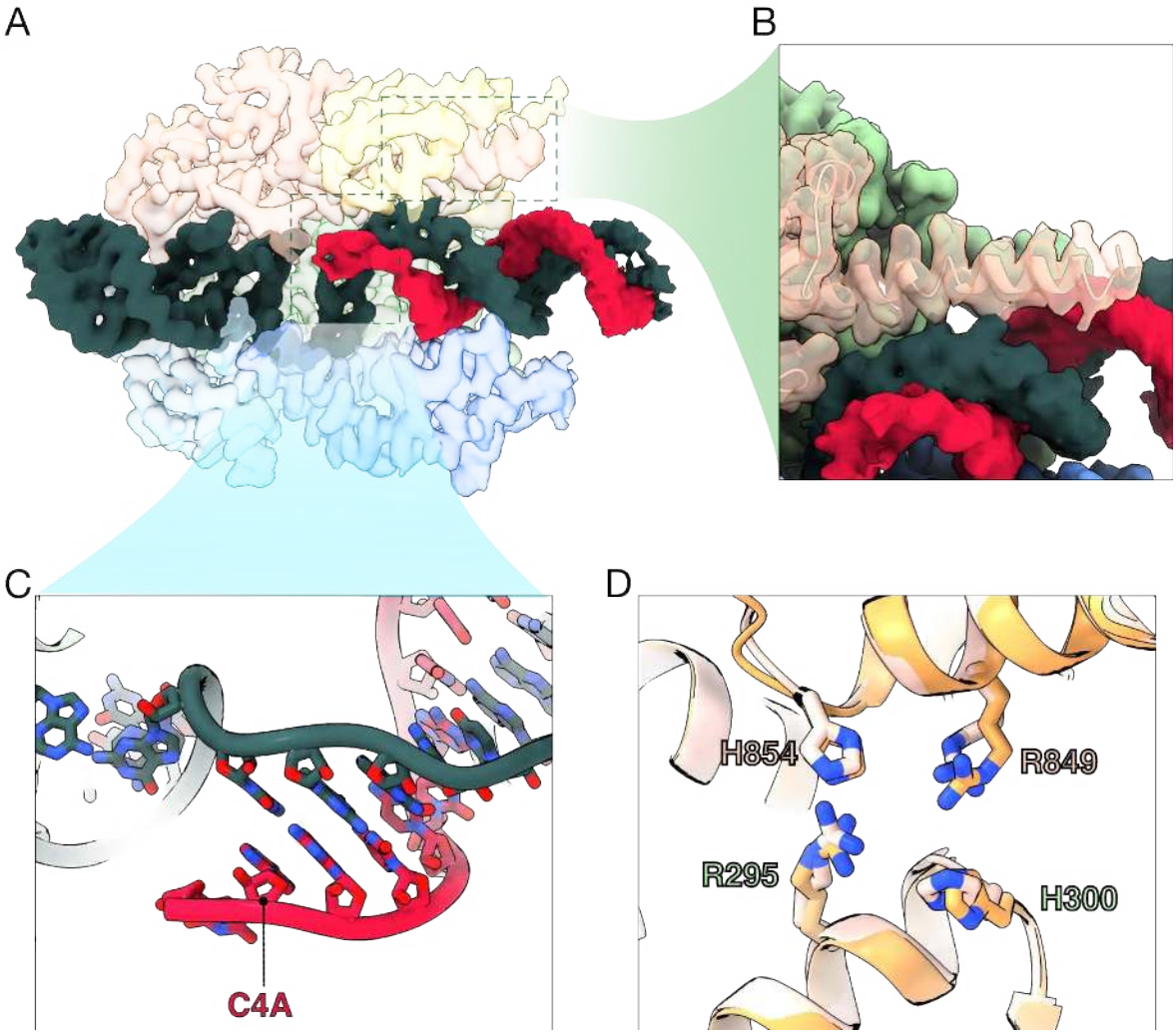

Figure S8: Structural features of the inactive state. (A) EM density of the Cas13d ternary inactive state (C4A target), colored by domains. Green: crRNA, Red: partial target RNA, Pink: HEPN2 domain, Yellow: Helical-2 domain, Light blue: NTD domain, Dark blue: Helical-1 domain. (B) Enlarged view of an elongated α-helix in the HEPN2 domain. (C) Enlarged view of the RNA duplex with missing base pairing at the proximal end, near the C4A mismatch. (D) Enlarged view of the nuclease active site in the inactive state (pink) overlapped with the binary structure from this study (orange).

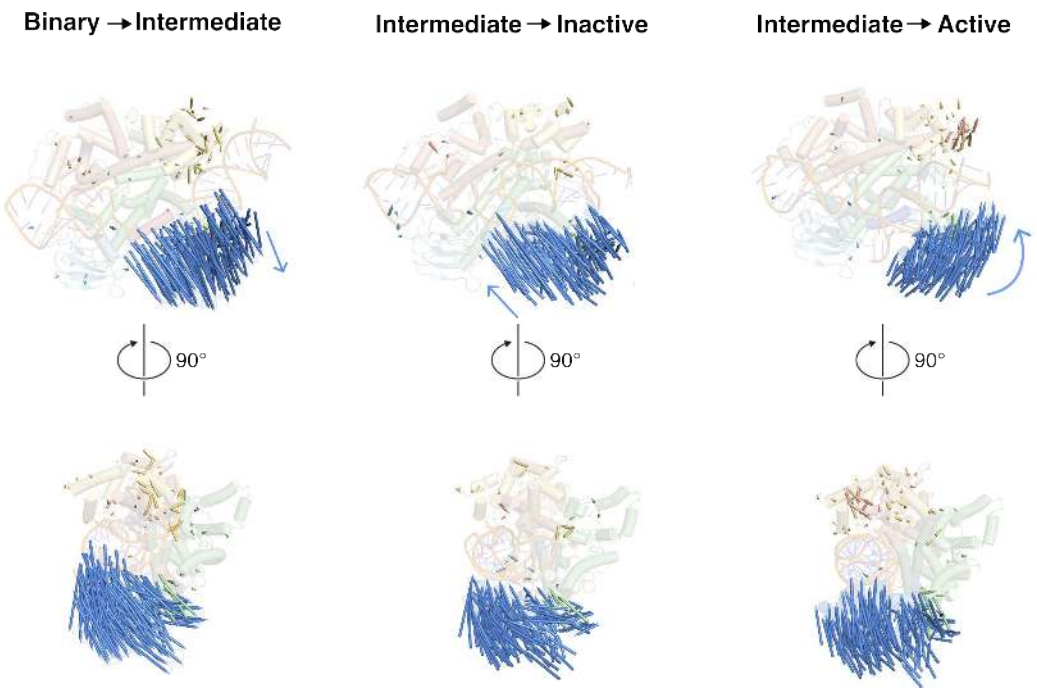

Figure S9: Conformational changes between the binary, intermediate, inactive, and active states. Transparent cartoon representations of binary (left), intermediate (middle), and active (right) states of Cas13d with vector arrows indicating the conformational changes of Cas13d upon target binding and activation. Blue arrows represent the vector direction of the Helical-1 domain.

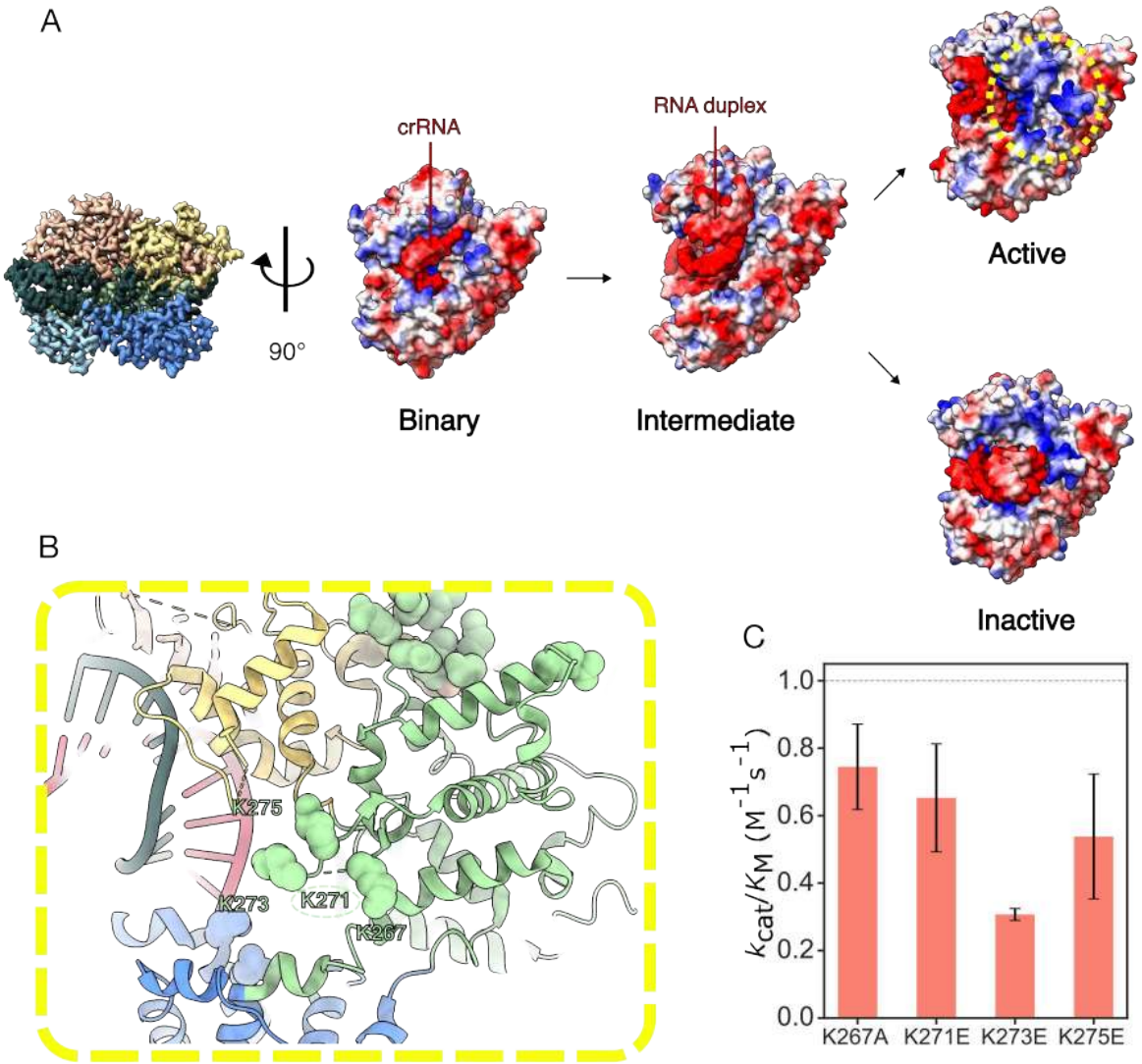

Figure S10: Cas13d activation reveals a positive-charge tunnel between Helical-2 and HEPN1 domain. (A) Electrostatic surfaces of Cas13d from different states. The dashed circle highlights the exposed positive charge in the active state. (B) Enlarged view of the exposed HEPN1 domain positive residues in the active state. (C) Cleavage activity of the indicated mutants in the positive charge tunnel. Error bars: mean and SEM from 3 independent experiments.

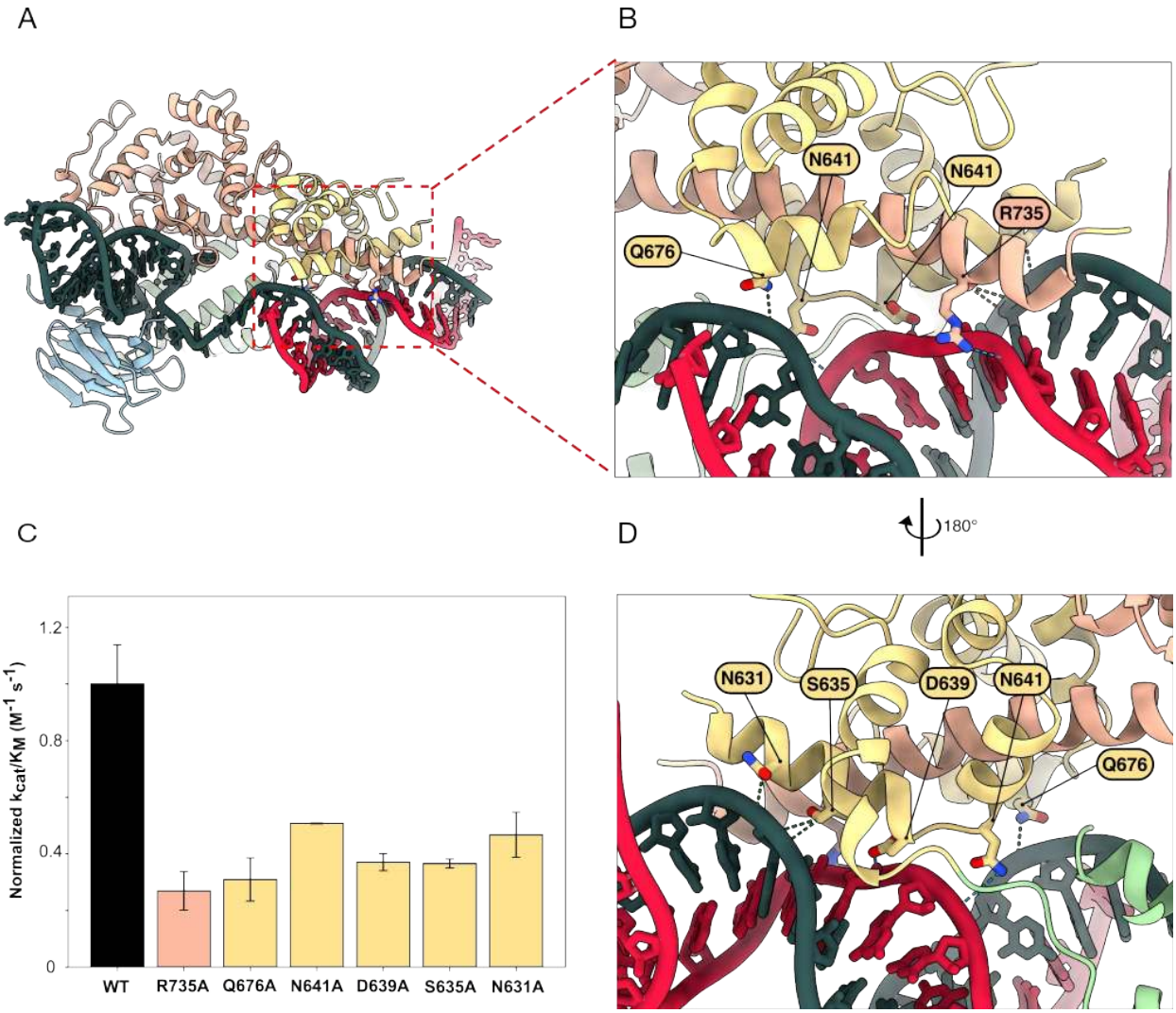

Figure S11: Residues involved in intermediate state stabilization are required for efficient Cas13d activation. (A) Structural overview of the Cas13d intermediate state bound to a matched target. The complex is colored by domain: NTD (light blue), Helical-1 (dark blue), HEPN1 (green), Helical-2 (yellow), and HEPN2 (pink). (B) Detailed view highlighting the interaction network between Cas13d residues and the RNA duplex. Residues selected for structure-guided alanine mutagenesis (R735, Q676, N641, D639, S635, and N631) form critical domain-domain and protein-RNA contacts that characterize this state. Hydrogen bonds are indicated by dashed lines. (C) Second-order cleavage rates (k_{cat}/K_M) of a trans substrate for WT and intermediate-stabilizing mutants, normalized to WT activity. All alanine substitutions significantly reduce cleavage efficiency, validating the role of these residues in mediating the transition from the intermediate checkpoint to the active state. Error bars: S.D. from three independent biological replicates. (D) 180° rotation of the view in (B), showing additional contacts. Colors in (B–D) represent domains, as in (A).

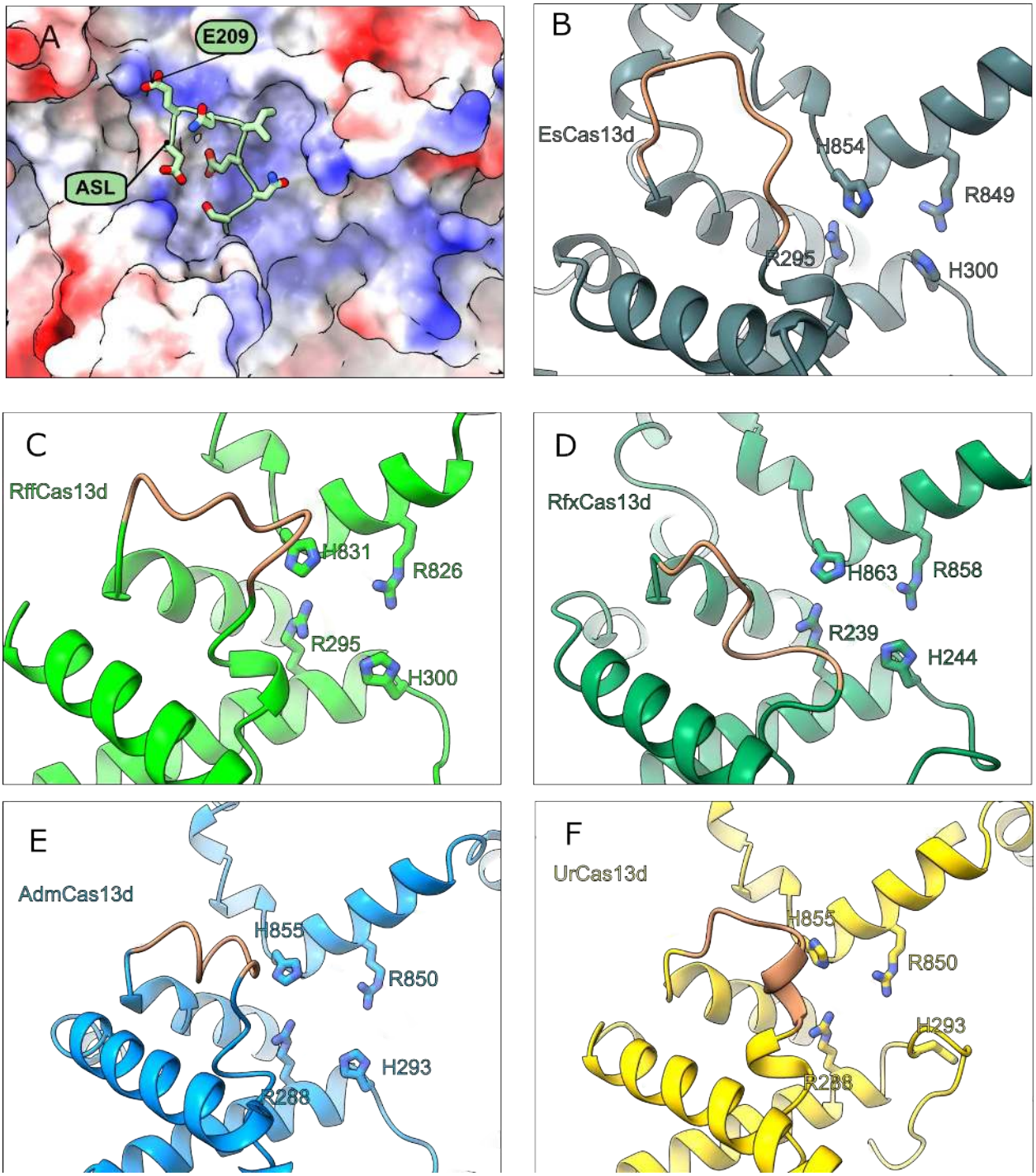

Figure S12: AlphaFold3-predicted structures of multiple Cas13d orthologs suggest that the active site loop (ASL) is conserved. (A) Enlarged views of ASL adjacent to the active site are shown on the electrostatic surface. (B-F) ASL and active sites in the Cas13 orthologs. Salmon: ASLs. The key active site residues are indicated explicitly.

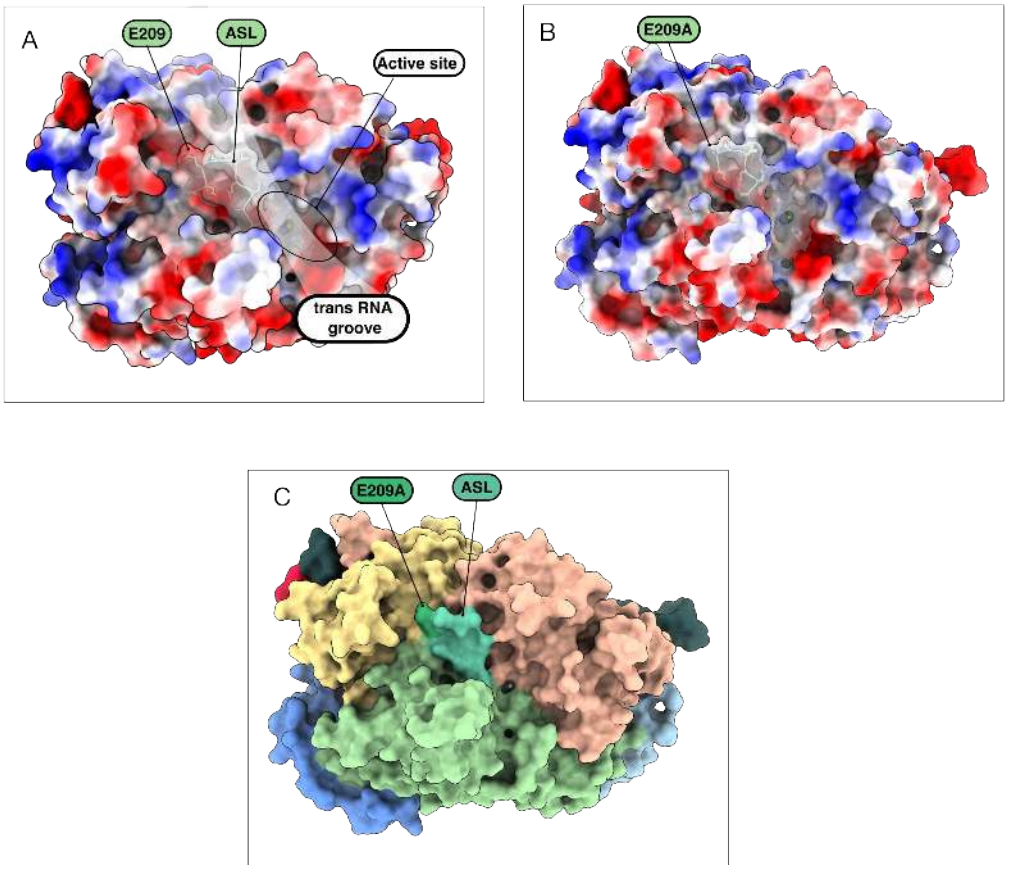

Figure S13: WT Cas13d surface charge and trans-RNA binding groove. (A) Electrostatic surface potential of WT Cas13d highlighting the trans-RNA binding groove and the position of the ASL gatekeeper. (B) Transparent representation of ASL with E209A mutation. (C) Surface representation of Cas13d. ASL is labeled in dim green.

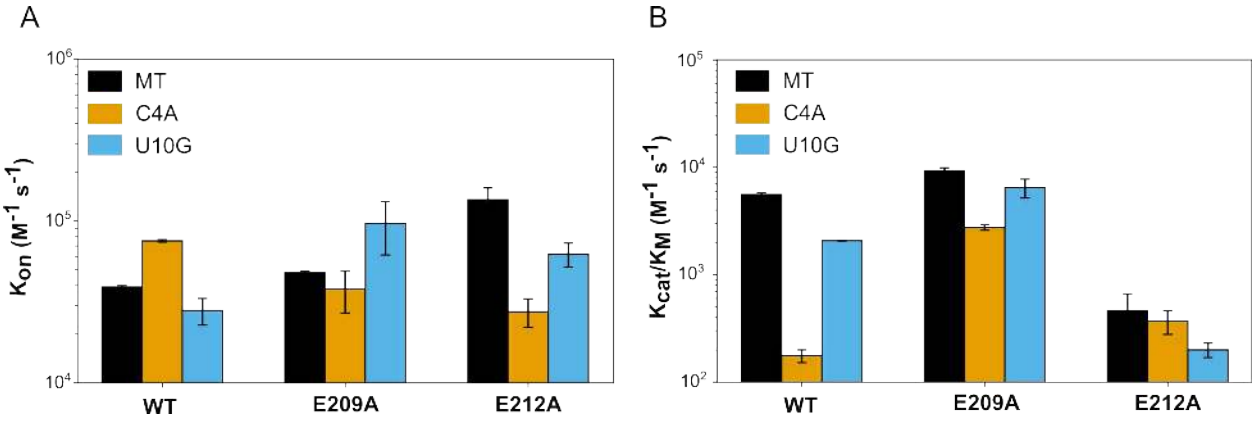

Figure S14: ASL mutants lose specificity at mispaired target RNAs. (A) Target binding rates (k_{on}) and (B) cleavage efficiencies (k_{cat}/K_M) were measured for a MT and mismatches (C4A, U10G). Bars show mean values; error bars indicate SD. Note that the hyperactivating E209A ASL mutant also increases binding and cleavage at mismatched targets.

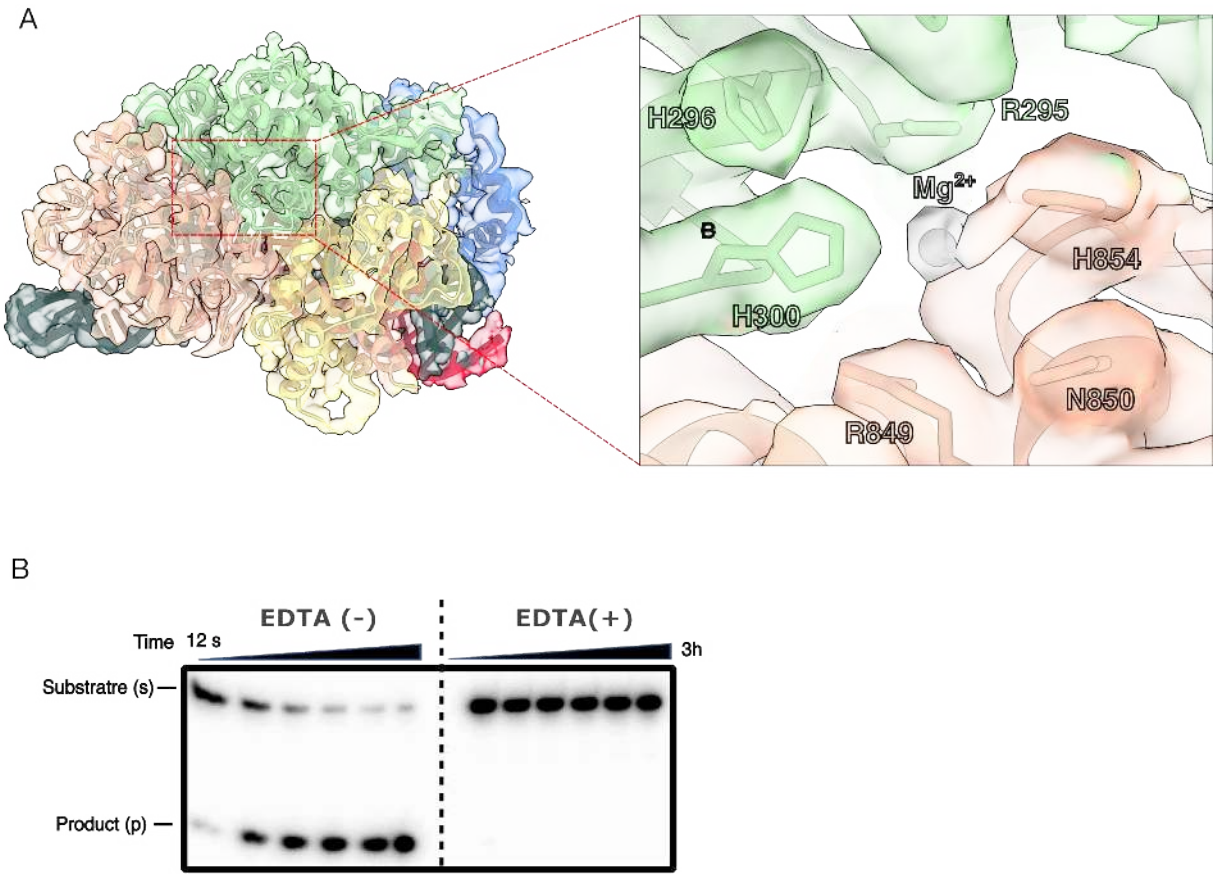

Figure S15: A potential cation is observed near the active site. (A) Cryo-EM structure of the active site highlighting the potential cation (grey). A potential cation is coordinated by the HEPN nuclease motif (RϕXXXH). (B) Gel showing time-course of trans-RNA cleavage in the presence (right) and absence (left) of EDTA. Cleavage occurs without EDTA, while no cleavage is observed with EDTA, indicating the essential role of metal ions in the cleavage reaction. Note that we cannot definitively conclude that Mg^{2+} is involved in the chemical cleavage step.

Supplemental Tables

Plasmid	Description	Source
pIF1023	6xHis-TwinStrep-SUMO-Cas13d	(26)
pIF1024	6xHis-TwinStrep-SUMO-dCas13d	(26)

Table S1: Plasmids used in this study.

Sample	Sequence
R1_crRNA	CACCCGUGCAAAAAUGCAGGGGUCUAAAACUGAGCGGAUAACCUCUCUAUGG
R2_MT_kinetic	GGGUUCGUACCAUAGAGAGGUUAUCCGCUCACCGAGAUCG
R3_C4A_kinetic	GGGUUCGUACCAUAGAGAGGUUAUCCGAUCACCGAGAUCG
R4_U10G_kinetic	GGGUUCGUACCAUAGAGAGGUGAUCCGCUCACCGAGAUCG
R5_MT_structure	CGUACCAUAGAGAGGUUAUCCGCUCACCGA
R6_C4A_structure	CGUACCAUAGAGAGGUUAUCCGAUCACCGA
R7_U10G_structure	CGUACCAUAGAGAGGUGAUCCGCUCACCGA
R8_Target-1(T1)	GGGUUCGUACCAUAGAGAGGUUAUCCGCUC
R9_Target-2(T2)	GGGUUCGUACCAUAGAGAGGUUAUCCGCUCA
R10_Target-3(T3)	GGGUUCGUACCAUAGAGAGGUUAUCCGCUCAC
R11_Target-4(T4)	GGGUUCGUACCAUAGAGAGGUUAUCCGCUCACC
R12_Target-5(T5)	GGGUUCGUACCAUAGAGAGGUUAUCCGCUCACCGA
R13_trans_substrate	GGGUUCGUAC
R14_trans_4'dU_substrate	GGGdUUCGUAC
R15_trans_5'dU_substrate	GGGUdUCGUAC
R16_trans_4',5'dU_substrate	GGGdUdUCGUAC
R17_crRNA2	CACCCGUGCAAAAUUGCAGGGGUCUAAAACUUUUGGUUGACCACAUCUUGAA
R18_MT2_kinetic	UUGGAAAACUUCAAGAUGUGGUCAACCAAAAUGCACAAGC
R19_crRNA3	CACCCGUGCAAAAUUGCAGGGGUCUAAAACCUUGAAGUUUUCCAAGUGCACU
R20_MT3_kinetic	UCCACAGCAAGUGCACUUGGAAAACUUCAAGAUGUGGUCA

Table S2: RNA sequences used in this study.

	Binary complex of EsCas13d (EMDB-47892) (PDB-9EBU)
Data collection and Processing	
Magnification	29,000
Voltage (kV)	200
Electron exposure (e^{-}/Å^2)	80
Defocus range (μm)	-1.2 to -2.2
Pixel size (Å)	0.81
Symmetry imposed	C1
Initial particle images (no.)	1,248k
Final particle images (no.)	192k
Map resolution (Å)	3.06
FSC threshold = 0.143	
Map resolution range (Å)	3-7
Refinement	
Initial model used (PDB code)	6E9E
Model resolution (Å)	3.1
FSC threshold	0.5
Model composition	
Non-hydrogen atoms	8097
Protein residues	860
Nucleotides	49
B factors (Å^2)	
Protein	44.30
Ligand	58.66
R.m.s. deviations	
Bond lengths (Å)	0.005
Bond angles (°)	0.631
Validation	
MolProbity score	2.38
Clashscore	7.88
Poor rotamers (%)	3.73
Ramachandran plot	
Favored (%)	97.64
Allowed (%)	2.36
Disallowed (%)	0.00

Table S3: EsCas13d binary complex Cryo-EM data collection and processing statistics

	EsCas13d with matched target	
	Intermediate state (EMDB-47903) (PDB-9EC9)	Active state (EMDB-47902) (PDB-9EC8)
Data collection and Processing		
Magnification	28,000	28,000
Voltage (kV)	300	300
Electron exposure (e^{-}/Å^2)	80	80
Defocus range (μm)	-1.2 to -2.2	-1.2 to -2.2
Pixel size (Å)	0.8332	0.8332
Symmetry imposed	C1	C1
Initial particle images (no.)	1377k	1377k
Final particle images (no.)	157k	176k
Map resolution (Å)	3.07	3.26
FSC threshold	0.143	0.143
Map resolution range (Å)	3 - 7	3 - 7
Refinement		
Initial model used (PDB code)	6E9F	6E9F
Model resolution (Å)	3.3	3.1
FSC threshold	0.5	0.5
Model composition		
Non-hydrogen atoms	7006	8663
Protein residues	676	861
Nucleotides	69	75
B factors (Å^2)		
Protein	72.85	90.90
Nucleotide	130.50	103.56
R.m.s. deviations		
Bond lengths (Å)	0.004	0.003
Bond angles (°)	0.864	0.567
Validation		
MolProbity score	1.54	1.38
Clashscore	7.39	6.95
Poor rotamers (%)	0.33	0.26
Ramachandran plot		
Favored (%)	97.58	98.12
Allowed (%)	2.42	1.88
Disallowed (%)	0.00	0.00

Table S4: EsCas13d-MT ternary complex Cryo-EM data collection and processing statistics

	EsCas13d with C4A target	
	Intermediate state (EMDB-47904) (PDB-9ECA)	Inactive state (EMDB-47908) (PDB-9ECE)
Data collection and Processing		
Magnification	28,000	28,000
Voltage (kV)	300	300
Electron exposure (e^{-}/Å^2)	80	80
Defocus range (μm)	-1.2 to -2.2	-1.2 to -2.2
Pixel size (Å)	0.8332	0.8332
Symmetry imposed	C1	C1
Initial particle images (no.)	3619k	3619k
Final particle images (no.)	235k	237k
Map resolution (Å)	3.19	3.01
FSC threshold	0.143	0.143
Map resolution range (Å)	3 - 7	3 - 7
Refinement		
Initial model used (PDB code)	6E9F	6E9F
Model resolution (Å)	3.4	3.1
FSC threshold	0.5	0.5
Model composition		
Non-hydrogen atoms	6918	8299
Protein residues	670	835
Nucleotides	67	68
B factors (Å^2)		
Protein	81.25	91.82
Nucleotide	146.62	144.89
R.m.s. deviations		
Bond lengths (Å)	0.003	0.003
Bond angles (°)	0.769	0.550
Validation		
MolProbity score	1.92	1.67
Clashscore	9.42	9.77
Poor rotamers (%)	1.67	1.60
Ramachandran plot		
Favored (%)	96.33	98.05
Allowed (%)	3.67	1.95
Disallowed (%)	0.00	0.00

Table S5: EsCas13d-C4A ternary complex cryo-EM data collection and processing statistics

	EsCas13d with U10G		
	Intermediate (EMDB-47905) (PDB-9ECB)	Inactive state (EMDB-47906) (PDB-9ECC)	Active state (EMDB-47907) (PDB-9ECD)
Data collection and Processing			
Magnification	28,000	28,000	28,000
Voltage (kV)	200	200	200
Electron exposure (e^{-}/Å^2)	80	80	80
Defocus range (μm)	-1.2 to -2.2	-1.2 to -2.2	-1.2 to -2.2
Pixel size (Å)	0.8332	0.8332	0.8332
Symmetry imposed	C1	C1	C1
Initial particle images (no.)	1777k	1777k	1777k
Final particle images (no.)	136k	125k	196k
Map resolution (Å)	3.15	3.32	3.47
FSC threshold	0.143	0.143	0.143
Map resolution range (Å)	3 - 7	3 - 7	3 - 7
Refinement			
Initial model used (PDB code)	6E9F	6E9F	6E9F
Model resolution (Å)	3.1	3.1	3.6
FSC threshold	0.5	0.5	0.5
Model composition			
Non-hydrogen atoms	8162	8120	8143
Protein residues	832	831	821
Nucleotides	62	61	66
B factors (Å^2)			
Protein	70.79	88.13	118.92
Nucleotide	102.68	142.31	140.24
R.m.s. deviations			
Bond lengths (Å)	0.003	0.003	0.003
Bond angles (°)	0.823	0.616	0.593
Validation			
MolProbity score	1.49	1.60	1.60
Clashscore	6.01	7.65	6.56
Poor rotamers (%)	1.61	1.74	2.03
Ramachandran plot			
Favored (%)	97.07	98.29	98.02
Allowed (%)	2.80	1.71	1.98
Disallowed (%)	0.12	0.00	0.00

Table S6: EsCas13d-U10G ternary complex cryo-EM data collection and processing statistics.

REFERENCES

1. O. O. Abudayyeh, J. S. Gootenberg, S. Konermann, J. Joung, I. M. Slaymaker, D. B. T. Cox, S. Shmakov, K. S. Makarova, E. Semenova, L. Minakhin, K. Severinov, A. Regev, E. S. Lander, E. V. Koonin, F. Zhang, C2c2 is a single-component programmable RNA-guided RNA-targeting CRISPR effector. *Science* **353**, aaf5573 (2016).

2. A. A. Smargon, D. B. T. Cox, N. K. Pyzocha, K. Zheng, I. M. Slaymaker, J. S. Gootenberg, O. A. Abudayyeh, P. Essletzbichler, S. Shmakov, K. S. Makarova, E. V. Koonin, F. Zhang, Cas13b is a type VI-B CRISPR-associated RNA-guided RNase differentially regulated by accessory proteins Csx27 and Csx28. *Mol. Cell* **65**, 618–630.e7 (2017).

3. S. Konermann, P. Lotfy, N. J. Brideau, J. Oki, M. N. Shokhirev, P. D. Hsu, Transcriptome engineering with RNA-targeting type VI-D CRISPR effectors. *Cell* **173**, 665–676.e14 (2018).

4. W. X. Yan, S. Chong, H. Zhang, K. S. Makarova, E. V. Koonin, D. R. Cheng, D. A. Scott, Cas13d is a compact RNA-targeting type VI CRISPR effector positively modulated by a WYL-domain-containing accessory protein. *Mol. Cell* **70**, 327–339.e5 (2018).

5. A. East-Seletsky, M. R. O'Connell, S. C. Knight, D. Burstein, J. H. D. Cate, R. Tjian, J. A. Doudna, Two distinct RNase activities of CRISPR-C2c2 enable guide-RNA processing and RNA detection. *Nature* **538**, 270–273 (2016).

6. S. Kannan, H. Altae-Tran, X. Jin, V. J. Madigan, R. Oshiro, K. S. Makarova, E. V. Koonin, F. Zhang, Compact RNA editors with small Cas13 proteins. *Nat. Biotechnol.* **40**, 194–197 (2022).

7. B. A. Adler, M. I. Trinidad, D. Bellieny-Rabelo, E. Zhang, H. M. Karp, P. Skopintsev, B. W. Thornton, R. F. Weissman, P. H. Yoon, L. Chen, T. Hessler, A. R. Eggers, D. Colognori, R. Boger, E. E. Doherty, C. A. Tsuchida, R. V. Tran, L. Hofman, H. Shi, K. M. Wasko, Z. Zhou, C. Xia, M. J. Al-Shimary, J. R. Patel, V. C. J. X. Thomas, R. Pattali, M. J. Kan, A. Vardapetyan, A. Yang, A. Lahiri, M. F. Maxwell, A. G. Murdock, G. C. Ramit, H. R. Henderson, R. W. Calvert, R. S. Bamert, G. J. Knott, A. Lapinaite, P. Pausch, J. C. Cofsky, E. J. Sontheimer, B. Wiedenheft, P. C. Fineran, S. J. J. Brouns, D. G. Sashital, B. C. Thomas, C. T. Brown, D. S. A. Goltsman, R. Barrangou, V. Siksnys, J. F. Banfield, D. F. Savage, J. A.

Doudna, CasPEDIA Database: A functional classification system for class 2 CRISPR-Cas enzymes. *Nucleic Acids Res.* **52**, D590–D596 (2024).

8. M. R. O'Connell, Molecular mechanisms of RNA targeting by Cas13-containing type VI CRISPR-Cas systems. *J. Mol. Biol.* **431**, 66–87 (2019).

9. Y. Ai, D. Liang, J. E. Wilusz, CRISPR/Cas13 effectors have differing extents of off-target effects that limit their utility in eukaryotic cells. *Nucleic Acids Res.* **50**, e65 (2022).

10. A. Mahas, R. Aman, M. Mahfouz, CRISPR-Cas13d mediates robust RNA virus interference in plants. *Genome Biol.* **20**, 263 (2019).

11. K. Zhang, Z. Zhang, J. Kang, J. Chen, J. Liu, N. Gao, L. Fan, P. Zheng, Y. Wang, J. Sun, CRISPR/Cas13d-mediated microbial RNA knockdown. *Front. Bioeng. Biotechnol.* **8**, 856 (2020).

12. R. Gupta, A. Ghosh, R. Chakravarti, R. Singh, V. Ravichandiran, S. Swarnakar, D. Ghosh, Cas13d: A new molecular scissor for transcriptome engineering. *Front. Cell Dev. Biol.* **10**, 866800 (2022).

13. T. Tang, Y. Han, Y. Wang, H. Huang, P. Qian, Programmable system of Cas13-mediated RNA modification and its biological and biomedical applications. *Front. Cell Dev. Biol.* **9**, 677587 (2021).

14. D. B. T. Cox, J. S. Gootenberg, O. O. Abudayyeh, B. Franklin, M. J. Kellner, J. Joung, F. Zhang, RNA editing with CRISPR-Cas13. *Science* **358**, 1019–1027 (2017).

15. O. O. Abudayyeh, J. S. Gootenberg, P. Essletzbichler, S. Han, J. Joung, J. J. Belanto, V. Verdine, D. B. T. Cox, M. J. Kellner, A. Regev, E. S. Lander, D. F. Voytas, A. Y. Ting, F. Zhang, RNA targeting with CRISPR–Cas13. *Nature* **550**, 280–284 (2017).

16. X. Qiao, Y. Gao, J. Li, Z. Wang, H. Qiao, H. Qi, Sensitive analysis of single nucleotide variation by Cas13d orthologs, EsCas13d and RspCas13d. *Biotechnol. Bioeng.* **118**, 3037–3045 (2021).

17. R. Nakagawa, S. Kannan, H. Altae-Tran, S. N. Takeda, A. Tomita, H. Hirano, T. Kusakizako, T. Nishizawa, K. Yamashita, F. Zhang, H. Nishimasu, O. Nureki, Structure and engineering of the minimal type VI CRISPR-Cas13bt3. *Mol. Cell* **82**, 3178–3192.e5 (2022).

18. C. Zhang, S. Konermann, N. J. Brideau, P. Lotfy, X. Wu, S. J. Novick, T. Strutzenberg, P. R. Griffin, P. D. Hsu, D. Lyumkis, Structural basis for the RNA-guided ribonuclease activity of CRISPR-Cas13d. *Cell* **175**, 212–223.e17 (2018).

19. X. Deng, E. Osikpa, J. Yang, S. J. Oladeji, J. Smith, X. Gao, Y. Gao, Structural basis for the activation of a compact CRISPR-Cas13 nuclease. *Nat. Commun.* **14**, 5845 (2023).

20. C. Xu, Y. Zhou, Q. Xiao, B. He, G. Geng, Z. Wang, B. Cao, X. Dong, W. Bai, Y. Wang, X. Wang, D. Zhou, T. Yuan, X. Huo, J. Lai, H. Yang, Programmable RNA editing with compact CRISPR–Cas13 systems from uncultivated microbes. *Nat. Methods* **18**, 499–506 (2021).

21. A. M. Molina Vargas, S. Sinha, R. Osborn, P. R. Arantes, A. Patel, S. Dewhurst, D. J. Hardy, A. Cameron, G. Palermo, M. R. O'Connell, New design strategies for ultra-specific CRISPR-Cas13a-based RNA detection with single-nucleotide mismatch sensitivity. *Nucleic Acids Res.* **52**, 921–939 (2024).

22. F. J. M. Mojica, C. Díez-Villaseñor, J. García-Martínez, C. Almendros, Short motif sequences determine the targets of the prokaryotic CRISPR defence system. *Microbiology* **155**, 733–740 (2009).

23. S. A. Shah, S. Erdmann, F. J. Mojica, R. A. Garrett, Protospacer recognition motifs: Mixed identities and functional diversity. *RNA Biol.* **10**, 891–899 (2013).

24. H.-H. Wessels, A. Méndez-Mancilla, X. Guo, M. Legut, Z. Daniloski, N. E. Sanjana, Massively parallel Cas13 screens reveal principles for guide RNA design. *Nat. Biotechnol.* **38**, 722–727 (2020).

25. H.-H. Wessels, A. Stirn, A. Méndez-Mancilla, E. J. Kim, S. K. Hart, D. A. Knowles, N. E. Sanjana, Prediction of on-target and off-target activity of CRISPR–Cas13d guide RNAs using deep learning. *Nat. Biotechnol.* **42**, 628–637 (2024).

26. H.-C. Kuo, J. Prupes, C.-W. Chou, I. J. Finkelstein, Massively parallel profiling of RNA-targeting CRISPR-Cas13d. *Nat. Commun.* **15**, 498 (2024).

27. P. B. Otoupal, B. F. Cress, J. A. Doudna, J. S. Schoeniger, CRISPR-RNAa: Targeted activation of translation using dCas13 fusions to translation initiation factors. *Nucleic Acids Res.* **50**, 8986–8998 (2022).

28. V. Tieu, E. Sotillo, J. R. Bjelajac, C. Chen, M. Malipatlolla, J. A. Guerrero, P. Xu, P. J. Quinn, C. Fisher, D. Klysz, C. L. Mackall, L. S. Qi, A versatile CRISPR-Cas13d platform for multiplexed transcriptomic regulation and metabolic engineering in primary human T cells. *Cell* **187**, 1278–1295.e20 (2024).

29. Z. Cui, C. Zeng, F. Huang, F. Yuan, J. Yan, Y. Zhao, Y. Zhou, W. Hankey, V. X. Jin, J. Huang, H. F. Staats, J. I. Everitt, G. D. Sempowski, H. Wang, Y. Dong, S.-L. Liu, Q. Wang, Cas13d knockdown of lung protease Ctsl prevents and treats SARS-CoV-2 infection. *Nat. Chem. Biol.* **18**, 1056–1064 (2022).

30. P. Yang, Y. Lou, Z. Geng, Z. Guo, S. Wu, Y. Li, K. Song, T. Shi, S. Zhang, J. Xiong, A. F. Chen, D. Li, W. T. Pu, L. Da, Y. Zhang, K. Sun, B. Zhang, Allele-specific suppression of variant MHC with high-precision RNA nuclease CRISPR-Cas13d prevents hypertrophic cardiomyopathy. *Circulation* **150**, 283–298 (2024).

31. J. E. Powell, C. K. W. Lim, R. Krishnan, T. X. McCallister, C. Saporito-Magriña, M. A. Zeballos, G. D. McPheron, T. Gaj, Targeted gene silencing in the nervous system with CRISPR-Cas13. *Sci. Adv.* **8**, eabk2485 (2022).

32. C.-C. Shen, M.-W. Lin, B. K. T. Nguyen, C.-W. Chang, J.-R. Shih, M. T. T. Nguyen, Y.-H. Chang, Y.-C. Hu, CRISPR-Cas13d for gene knockdown and engineering of CHO cells. *ACS Synth. Biol.* **9**, 2808–2818 (2020).

33. M. D. Schertzer, A. Stirn, K. Isaev, L. Pereira, S. H. Park, A. Das, A. Réal, E. D. Jeffery, C. Harbison, H. Wessels, G. M. Sheynkman, N. E. Sanjana, D. A. Knowles, Cas13d-mediated isoform-specific RNA knockdown with a unified computational and experimental toolbox. *Nat. Commun.* **16**, 6948 (2025).

34. S. K. Hart, S. Müller, H.-H. Wessels, A. Méndez-Mancilla, G. Drabavicius, O. Choi, N. E. Sanjana, Precise RNA targeting with CRISPR-Cas13d. *Nat. Biotechnol.* **44**, 64–69 (2026).

35. A. Tambe, A. East-Seletsky, G. J. Knott, J. A. Doudna, M. R. O'Connell, RNA binding and HEPN-nuclease activation are decoupled in CRISPR-Cas13a. *Cell Rep.* **24**, 1025–1036 (2018).

36. J. Yang, Y. Song, X. Deng, J. A. Vanegas, Z. You, Y. Zhang, Z. Weng, L. Avery, K. D. Dieckhaus, A. Peddi, Y. Gao, Y. Zhang, X. Gao, Engineered LwaCas13a with enhanced collateral activity for nucleic acid detection. *Nat. Chem. Biol.* **19**, 45–54 (2023).

37. B. Zhang, Y. Ye, W. Ye, V. Perčulija, H. Jiang, Y. Chen, Y. Li, J. Chen, J. Lin, S. Wang, Q. Chen, Y.-S. Han, S. Ouyang, Two HEPN domains dictate CRISPR RNA maturation and target cleavage in Cas13d. *Nat. Commun.* **10**, 2544 (2019).

38. J. Wei, P. Lotfy, K. Faizi, S. Baungaard, E. Gibson, E. Wang, H. Slabodkin, E. Kinnaman, S. Chandrasekaran, H. Kitano, M. G. Durrant, C. V. Duffy, A. Pawluk, P. D. Hsu, S. Konermann, Deep learning and CRISPR-Cas13d ortholog discovery for optimized RNA targeting. *Cell Syst.* **14**, 1087–1102.e13 (2023).

39. H. Yang, D. J. Patel, Structures, mechanisms and applications of RNA-centric CRISPR–Cas13. *Nat. Chem. Biol.* **20**, 673–688 (2024).

40. M. Pacesa, C.-H. Lin, A. Cléry, A. Saha, P. R. Arantes, K. Bargsten, M. J. Irby, F. H. Allain, G. Palermo, P. Cameron, P. D. Donohoue, M. Jinek, Structural basis for Cas9 off-target activity. *Cell* **185**, 4067–4081.e21 (2022).

41. E. N. Nikolova, H. Zhou, F. L. Gottardo, H. S. Alvey, I. J. Kimsey, H. M. Al-Hashimi, A historical account of Hoogsteen base-pairs in duplex DNA. *Biopolymers* **99**, 955–968 (2013).

42. N. B. Leontis, J. Stombaugh, E. Westhof, The non-Watson–Crick base pairs and their associated isostericity matrices. *Nucleic Acids Res.* **30**, 3497–3531 (2002).

43. S. Gao, H. Guan, H. Bloomer, D. Wich, D. Song, J. Khirallah, Z. Ye, Y. Zhao, M. Chen, C. Xu, L. Liu, Q. Xu, Harnessing non-Watson-Crick's base pairing to enhance CRISPR effectors

cleavage activities and enable gene editing in mammalian cells. *Proc. Natl. Acad. Sci. U.S.A.* **121**, e2308415120 (2023).

44. B. Wang, T. Zhang, J. Yin, Y. Yu, W. Xu, J. Ding, D. J. Patel, H. Yang, Structural basis for self-cleavage prevention by tag:anti-tag pairing complementarity in type VI Cas13 CRISPR systems. *Mol. Cell* **81**, 1100–1115.e5 (2021).

45. A. J. Meeske, S. Nakandakari-Higa, L. A. Marraffini, Cas13-induced cellular dormancy prevents the rise of CRISPR-resistant bacteriophage. *Nature* **570**, 241–245 (2019).

46. M. C. Pillon, J. Gordon, M. N. Frazier, R. E. Stanley, HEPN RNases—An emerging class of functionally distinct RNA processing and degradation enzymes. *Crit. Rev. Biochem. Mol. Biol.* **56**, 88–108 (2021).

47. M. C. Pillon, M. Sobhany, R. E. Stanley, Characterization of the molecular crosstalk within the essential Grc3/Las1 pre-rRNA processing complex. *RNA* **24**, 721–738 (2018).

48. M. Shigematsu, T. Kawamura, Y. Kirino, Generation of 2',3'-cyclic phosphate-containing RNAs as a hidden layer of the transcriptome. *Front. Genet.* **9**, 562 (2018).

49. V. Anantharaman, K. S. Makarova, A. M. Burroughs, E. V. Koonin, L. Aravind, Comprehensive analysis of the HEPN superfamily: Identification of novel roles in intra-genomic conflicts, defense, pathogenesis and RNA processing. *Biol. Direct* **8**, 15 (2013).

50. L. Liu, X. Li, J. Ma, Z. Li, L. You, J. Wang, M. Wang, X. Zhang, Y. Wang, The molecular architecture for RNA-guided RNA cleavage by Cas13a. *Cell* **170**, 714–726.e10 (2017).

51. A. Shen, Allosteric regulation of protease activity by small molecules. *Mol. Biosyst.* **6**, 1431–1443 (2010).

52. J. Hu, L. G. Ahuja, H. S. Meharena, N. Kannan, A. P. Kornev, S. S. Taylor, A. S. Shaw, Kinase regulation by hydrophobic spine assembly in cancer. *Mol. Cell. Biol.* **35**, 264–276 (2015).

53. P. Shi, M. R. Murphy, A. O. Aparicio, J. S. Kesner, Z. Fang, Z. Chen, A. Trehan, Y. Guo, X. Wu, Collateral activity of the CRISPR/RfxCas13d system in human cells. *Commun. Biol.* **6**, 334 (2023).

54. C. P. Kelley, M. C. Haerle, E. T. Wang, Negative autoregulation mitigates collateral RNase activity of repeat-targeting CRISPR-Cas13d in mammalian cells. *Cell Rep.* **40**, 111226 (2022).

55. H. Tong, J. Huang, Q. Xiao, B. He, X. Dong, Y. Liu, X. Yang, D. Han, Z. Wang, X. Wang, W. Ying, R. Zhang, Y. Wei, C. Xu, Y. Zhou, Y. Li, M. Cai, Q. Wang, M. Xue, G. Li, K. Fang, H. Zhang, H. Yang, High-fidelity Cas13 variants for targeted RNA degradation with minimal collateral effects. *Nat. Biotechnol.* **41**, 108–119 (2023).

56. D. N. Mastronarde, SerialEM: A program for automated tilt series acquisition on Tecnai microscopes using prediction of specimen position. *Microsc. Microanal.* **9**, 1182–1183 (2003).

57. A. Punjani, J. L. Rubinstein, D. J. Fleet, M. A. Brubaker, cryoSPARC: Algorithms for rapid unsupervised cryo-EM structure determination. *Nat. Methods* **14**, 290–296 (2017).

58. P. D. Adams, P. V. Afonine, G. Bunkóczi, V. B. Chen, I. W. Davis, N. Echols, J. J. Headd, L.-W. Hung, G. J. Kapral, R. W. Grosse-Kunstleve, A. J. McCoy, N. W. Moriarty, R. Oeffner, R. J. Read, D. C. Richardson, J. S. Richardson, T. C. Terwilliger, P. H. Zwart, PHENIX: A comprehensive Python-based system for macromolecular structure solution. *Acta Crystallogr. D Biol. Crystallogr.* **66**, 213–221 (2010).

59. T. I. Croll, ISOLDE: A physically realistic environment for model building into low-resolution electron-density maps. *Acta Crystallogr. D Struct. Biol.* **74**, 519–530 (2018).

60. P. Emsley, B. Lohkamp, W. G. Scott, K. Cowtan, Features and development of Coot. *Acta Crystallogr. D Biol. Crystallogr.* **66**, 486–501 (2010).

61. A. Punjani, H. Zhang, D. J. Fleet, Non-uniform refinement: Adaptive regularization improves single-particle cryo-EM reconstruction. *Nat. Methods* **17**, 1214–1221 (2020).